

See discussions, stats, and author profiles for this publication at: <https://www.researchgate.net/publication/231645696>

Graphene Nanoflakes: Thermal Stability, Infrared Signatures, and Potential Applications in the Field of Spintronics and Optical Nanodevices

ARTICLE *in* THE JOURNAL OF PHYSICAL CHEMISTRY C · SEPTEMBER 2010

Impact Factor: 4.77 · DOI: 10.1021/jp105728p

CITATIONS

38

READS

80

3 AUTHORS, INCLUDING:



[Freire Valder](#)

Universidade Federal do Ceará

295 PUBLICATIONS 1,838 CITATIONS

[SEE PROFILE](#)

Graphene Nanoflakes: Thermal Stability, Infrared Signatures, and Potential Applications in the Field of Spintronics and Optical Nanodevices

A. M. Silva, M. S. Pires, and V. N. Freire

Departamento de Física, Universidade Federal do Ceará, Caixa Postal 6030,
60455-900 Fortaleza, Ceará, Brazil

E. L. Albuquerque

Departamento de Biofísica e Farmacologia, Universidade Federal do Rio Grande do Norte,
59072-900 Natal, Rio Grande do Norte, Brazil

D. L. Azevedo

Departamento de Física, Centro Tecnológico, Universidade Federal do Maranhão,
65085-580 São Luís, Maranhão, Brazil

E. W. S. Caetano*

Instituto Federal de Educação, Ciência e Tecnologia do Ceará, Av. 13 de Maio, 2081, Benfica,
60040-531 Fortaleza, Ceará, Brazil

Received: June 21, 2010; Revised Manuscript Received: August 21, 2010

We investigate the structural, electronic, and vibrational properties of graphene nanoflakes (GNFs) with a small number of atoms (<250) and distinct shapes (triangular, rectangular, and hexagonal) through classical molecular dynamics (CMD) and density functional theory (DFT) calculations. We show that these graphene nanostructures are able to retain their planarity for simulated temperatures up to 1500 K, starting to degrade into amorphous nanocarbon for temperatures above 3000 K. The shapes and types of border of the GNFs have a strong influence on their electronic properties and spin. The HOMO–LUMO energy gap of the studied nanoflakes spans the full range of the visible spectrum, suggesting potential applications in the fabrication of optical emission nanodevices, which is confirmed by TDDFT calculations to obtain the UV–vis absorption spectra of triangular armchair GNFs. In particular, the UV–vis maximum absorption energies and intensities scale linearly with the linear size of the GNF. In the special case of zigzag-edged triangular nanoflakes, a nonzero net spin which increases linearly with the edge size was found, pointing toward possible spintronic applications by tuning the spin distribution. The DFT calculations of the infrared spectra allowed the identification of shape- and border-related fingerprints.

I. Introduction

Graphene is the first example of a truly two-dimensional (2D) crystal,^{1,2} being a carbon-based zero-gap semiconductor whose charge carriers are more easily and naturally described through Dirac's equation rather than the Schrödinger equation.³ Graphene sheets are thermally and structurally stable, and can be isolated by mechanical cleavage of graphite samples.² The electronic structure of graphene-based nanostructures is different from bulk graphite because of surface and related edge effects.^{4,5} Graphene-based 2D nanostructures are hopeful candidates for the achievement of room-temperature ballistic transport on a submicrometer scale³ due to the high mobility of charge carriers in graphene.

Progress in this direction is the synthesis of carbon nanoribbons,⁶ which are elaborated stripes of single layered graphene with finite width. Berger et al.⁷ reported the synthesis of a thin graphite film on a SiC substrate and have shown that this material can be used to create patterns using nanolithography methods. The transport properties of the film were dominated by the graphene layer at the SiC interface, showing a great potential toward the development of electronic nanodevices. A chemical route to produce semiconducting graphene nanoribbons

with ultrasmooth edges was developed by Li et al.,⁸ affording the fabrication of graphene field effect transistors with on–off ratios at room temperature of about 10⁷. Transport measurements on etched graphene nanoribbons were performed, giving useful insights to understand the transport in graphene nanostructures.⁹ More recently, the anisotropic etching of single layer graphene was achieved, producing stable nanoribbons having widths smaller than 10 nm and providing a method to make graphene nanocircuits.¹⁰

Theoretical simulations of Z-shaped graphene nanoribbons revealed that a quantum dot can be trapped at the junction, with complete confinement of electronic states and allowing for a method to easily design quantum dot devices.¹¹ A quantum computation scheme based on Z-shaped graphene nanoribbons was also proposed,¹² with qubits encoded in electron or hole spin states localized at zigzag edges. Density functional theory (DFT) calculations using the PBE and HSE exchange-correlation functionals to assess the electronic structure and stability of semiconducting graphene nanoribbons showed that the main band gap oscillates as a function of the ribbon width (L).¹³ The largest oscillations were observed for $L < 1.0$ nm, reaching

variations of as much as 2.0 eV for H-terminated nanoribbons. Optical transition energies as well as the dielectric constant were also shown to be dependent on the width and on the passivation of dangling bonds at the edges.¹³ These results indicate that shape effects can affect the properties of small pieces of graphene. The influence of edge structure on the electronic properties of graphene quantum dots and nanoribbons was experimentally demonstrated through tunneling spectroscopy.⁵

Pursuing the route of graphene as an attractive nanoscale building block,^{3,14} mechanical or chemical splitting of graphite into small pieces with a small number n of atoms can give rise to graphene nanoflakes (GNFs), also called polycyclic aromatic hydrocarbons (PAHs), which are very promising for technological applications.^{2,4} Within the last two years, several theoretical works on GNFs were published. Tight-binding calculations were employed to investigate (i) the electronic structure of GNFs under magnetic fields,¹⁵ (ii) the inner and outer edge electronic states of hollow GNFs,¹⁶ (iii) the sliding friction of graphene flakes,¹⁷ (iv) the electronic structure of GNFs with different shapes near the Fermi level,^{18–20} and (v) the shell and supershell structure of electronic energy levels in triangular and circular graphene flakes.^{21,22} First-principles calculations within the density functional theory approach were also performed, for example, to study the thermal stability of GNFs ($n = 24, 32, 128$) for temperatures up to 2400 K,²³ and to investigate the spin-dependent quantum transport of hydrogen-terminated and vanadium functionalized GNFs.²⁴ Rectangular graphene nanodots (having both armchair and zigzag edges) with different edge chemical modifications were simulated employing the hybrid B3LYP exchange-correlation functional.²⁵ The saturation with different atoms or molecular groups on the zigzag edges leads to a spin-polarized ground state with magnetic moment, spin density, and electronic energy gap strongly dependent on the atomic groups used to passivate the dangling bonds. Nagai et al.²⁶ used density functional theory methods to study the second hyperpolarizabilities of hexagonal shaped graphene fragments with zigzag and armchair edges. Yoneda et al.,²⁷ afterward, used hybrid density functional theory to probe the relationship between the third-order nonlinear optical properties of trigonal, rhombic, and bow-tie GNFs, their diradical characters, and their spin multiplicities. Benzenoid graph theory and first-principles calculations were used to investigate the magnetic properties of graphene fragments with arbitrary shape, showing that the spin of a graphene nanoflake has a strong dependence on its shape due to topological frustration of π bonds.^{28,29} Graphene quantum dots have been studied through *ab initio* electronic calculations, being proposed as structures that can serve as the fundamental logic gates of high-density ultrafast spintronic devices.³⁰ Finally, other theoretical approaches were employed to improve the understanding of the confinement and transport of electrons in graphene quantum dots and the magnetic properties of these nanostructures.^{31–35}

On the experimental side, Shang et al.³⁶ reported the synthesis of multilayer GNF films through a microwave plasma enhanced chemical vapor deposition method. Their GNFs presented a highly graphitized knife-edge structure with thickness in the 2–3 nm range. Nanoflake films were proposed as a means to create a new class of nanostructured electrodes for biosensing and energy storage/conversion applications.³⁶ Very recently, a simple and effective method for the production of GNFs directly from graphite was demonstrated,³⁷ consisting of the mild ultrasonication of highly ordered pyrolytic graphite in the presence of appropriate surfactants. Characterization through scanning and transmission electron microscopy revealed that the dispersed

phase is formed mainly from layered GNFs with an average thickness of about 1 nm, with potential applications in the formation of conducting composite materials. Besides that, it was demonstrated that stable graphene nanostructures can be sculpted using electrom beams or scanning probes.^{38,39}

In this work, we study triangular, rectangular, and hexagonal GNFs (number of carbon atoms varying from 13 to 240) using two approaches: classical molecular dynamics (CMD) and first-principles calculations within the density functional theory (DFT) formalism. The first part of the paper is an investigation on the structural stability of a chosen set of nanoflakes for different temperatures through CMD and adopting a reactive empirical bond order (REBO) forcefield. We obtain that hydrogen-passivated zigzag borders give more thermal stability to the nanoflakes in contrast with hydrogen-passivated armchair borders. The thermal stability of GNFs up to 1500 K suggests their use in high temperature applications, competing with silicon carbide as a material for the development of hot gas sensors.⁴⁰ In the second part, the results of DFT geometry optimizations for several GNFs, as well as their electronic properties (electronic eigenenergies, HOMO–LUMO energy gaps, densities of states) are presented. We show that when the number of carbon atoms is small (<100), the nanoflake's shape and edge configuration is a very important factor affecting its structural, electronic, and vibrational properties. Our results suggest that it is feasible to use very small flakes of graphene or analogous structures patterned on graphene sheets to produce light emission covering the full visible spectrum. Vibrational frequencies and the infrared spectra for the nanoflakes used as inputs for the classical molecular dynamics simulations were also found, being shown that the infrared spectra allow the assignment of some peaks to a specific nanoflake geometry and edge type, and the consequent identification of nanoflake shape through infrared spectroscopy.

II. Describing GNF Shapes

The set of GNFs considered in our computations is formed from three basic shapes: equilateral triangle, rectangle, and regular hexagon. All edge dangling bonds were passivated with hydrogen. Triangular and hexagonal nanoflakes with armchair and zigzag edges are easily built from graphene sheets thanks to symmetry (see Figure 1, top and bottom). For the rectangular nanoflakes, we have taken into account the pattern shown in the middle part of Figure 1, with parallel armchair and zigzag borders. To specify the size of each GNF, we define a generation number N , which corresponds to the number of hexagonal motifs along an edge, counted for each shape as indicated in Figure 1 (one can note that the rectangular nanoflakes studied here always have the same number of hexagonal motifs along the armchair and zigzag edges, being roughly square). We will use the following abbreviations to specify the GNFs: TA for triangular with armchair border, TZ for triangular with zigzag border, R for rectangular, HA for hexagonal with armchair border, and HZ for hexagonal with zigzag border. These abbreviations followed by a number indicate the generation count N of the nanoflake. For example, HZ4 stands for hexagonal nanoflake with zigzag border and $N = 4$.

The number of carbon (hydrogen) atoms for each type of GNF is a second degree (first degree) polynomial of N , denoted $n_C(N)$ ($n_H(N)$). The polynomials for the sets of nanoflakes under study are displayed in Table 1. The rate of growth of n_C with N is the highest for the HA nanoflakes, being followed by the HZ, TA, R, and TZ nanoflakes in decreasing order. For the number of hydrogen atoms, n_H , the rate of growth with N follows

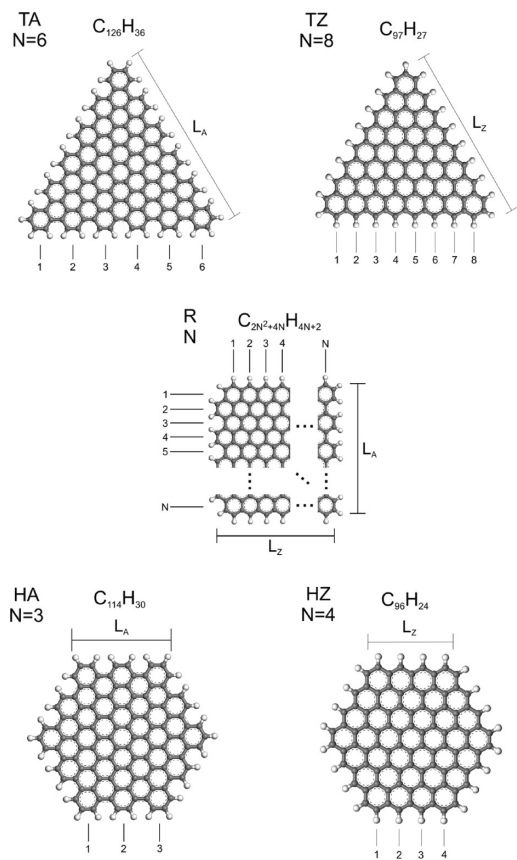


Figure 1. Triangular (top), rectangular (middle), and hexagonal (bottom) GNFs investigated in this work. Abbreviations, counting procedures and generation numbers, are also shown.

TABLE 1: Counting Formulae for the Number of Carbon Atoms ($n_C(N)$), Hydrogen Atoms ($n_H(N)$), and Carbon Hexagons ($h(N)$) for the GNFs Investigated in This Work^a

	$n_C(N)$	$n_H(N)$	$h(N)$
TA	$3N^2 + 3N$	$6N$	$(3N^2 - 3N + 2)/2$
TZ	$N^2 + 4N + 1$	$3N + 3$	$(N^2 + N)/2$
R	$2N^2 + 4N$	$4N + 2$	N^2
HA	$18N^2 - 18N + 6$	$12N - 6$	$9N^2 - 15N + 7$
HZ	$6N^2$	$6N$	$3N^2 - 3N + 1$
	L_A	L_Z	space group
TA	$3Nl$		D_{3h}
TZ		$\sqrt{3}(N + 1)l$	D_{3h}
R	$(1/2)(3N + 1)l$	$(\sqrt{3}/2)(2N + 1)l$	C_{2v} (odd N), C_{2h} (even N)
HA	$(3N - 2)l$		D_{6h}
HZ		$\sqrt{3}(N - 1/3)l$	D_{6h}

^a L_A and L_Z are size estimates associated with armchair and zigzag borders, respectively, as shown in Figure 1. l is the average C–C bond length. Symmetry point groups of the nanoflakes are also shown.

the sequence HA > HZ = TA > R > TZ. The number of carbon hexagons, $h(N)$, as for $n_C(N)$, is given by a second degree polynomial of N and its rate of growth for different GNFs follows the sequence HA > HZ > R > TA > TZ. The characteristic dimensions of each type of GNF are denoted here by L_A (armchair edge) and L_Z (zigzag edge), being linear functions of N and the average C–C bond length l (see Figure 1 and the bottom part of Table 1; for graphene, l is approximately 0.142 nm). Finally, the point groups of the GNFs are D_{3h} and D_{6h} for triangular and hexagonal shapes, respec-

tively. For the rectangular shapes, the point group is C_{2v} for odd values of N and C_{2h} for even values.

We have ran our computations for the following GNFs: TA with N varying from 2 to 8 (which means that L_A varies from 0.85 nm for $N = 2$ to 3.41 nm for $N = 8$, approximately), TZ with N varying from 2 to 13 (L_Z varying from 0.74 nm for $N = 2$ to 3.20 nm for $N = 13$), R with N varying from 2 to 10 (L_A varying from 0.50 nm for $N = 2$ to 2.20 nm for $N = 10$, L_Z varying from 0.61 nm for $N = 2$ to 2.58 nm for $N = 10$), HA with N varying from 2 to 4 (L_A varying from 0.57 nm for $N = 2$ to 1.42 nm for $N = 4$), and HZ with N in the 2–6 range (L_Z varying from 0.41 nm for $N = 2$ to 1.39 nm for $N = 6$). The $N = 1$ nanoflake is a benzene molecule. The smallest GNF (in number of atoms) we have investigated is TZ2, with chemical formula $C_{13}H_9$, and the largest one is R10, with chemical formula $C_{240}H_{42}$. The computational cost of calculations within the density functional theory (DFT) formalism prevented us from performing calculations for molecules with more than 300 atoms.

We carried out our study in two steps: first, a representative subset of graphene nanoflakes (TA4, TZ6, R4, HA2, and HZ3) was subjected to a classical molecular dynamics simulation to check for stability with increasing temperature. The Brenner REBO (reactive empirical bond order) forcefield,^{41,42} which allows for the formation and breaking of covalent bonds, was chosen to perform these computations. This forcefield gives a good description of bond energies, lengths, and force constants for hydrocarbon molecules, and provides a good agreement with first-principles calculations for the bulk elastic properties, defect energies, and surface energies of diamond. The NVT ensemble was adopted with temperature varying in the 1000–4200 K range, with an equilibration time of 5.0 ps, production time of 20.0 ps, and time step of 1.0 fs. The Nosé–Hoover thermostat was used with a thermostat parameter of 0.005.

The second step of the simulations was to perform geometry optimizations for all graphene nanoflakes (TA2–8, TZ2–13, R2–10, HA2–4, HZ2–6) within the density functional theory (DFT) formalism using the DMOL3 code.^{43,44} The generalized gradient approximation (GGA) for the exchange-correlation functional parametrized by Perdew and Wang was adopted,⁴⁵ with the double numerical plus polarization (DNP) basis set being used to expand the Kohn–Sham wave functions, and taking all electrons into account explicitly with unrestricted spin (for the sake of comparison, the DNP basis set is as accurate as the 6-311+G(3df,2pd) Gaussian basis set^{43,44,46}). The self-consistent field (SCF) tolerance was set to 10^{-6} Ha, and the electron density used as input for each SCF iteration was adjusted to be a mixture of 20% of the current density and 80% of the density calculated in the previous step. A DIIS (direct inversion in an iterative subspace) scheme was employed to speed up the SCF convergence. The process of geometry optimization was accomplished when the following thresholds were reached: (i) total energy variation smaller than 10^{-5} Ha, (ii) maximum force per atom smaller than 0.002 Ha/Å, and (iii) maximum atomic displacement smaller than 0.005 Å. The electronic eigenstates and electronic partial density of states are automatically found by DMOL3 after the end of the calculations. The vibrational normal modes and infrared spectra were also computed for the same subset of GNFs selected for the classical molecular dynamics step but using a different approach (see section IV).

III. GNF Structural Stability

The synthesis of GNFs is highly sensitive to their stability with temperature.^{23,47} It has been suggested that the formation

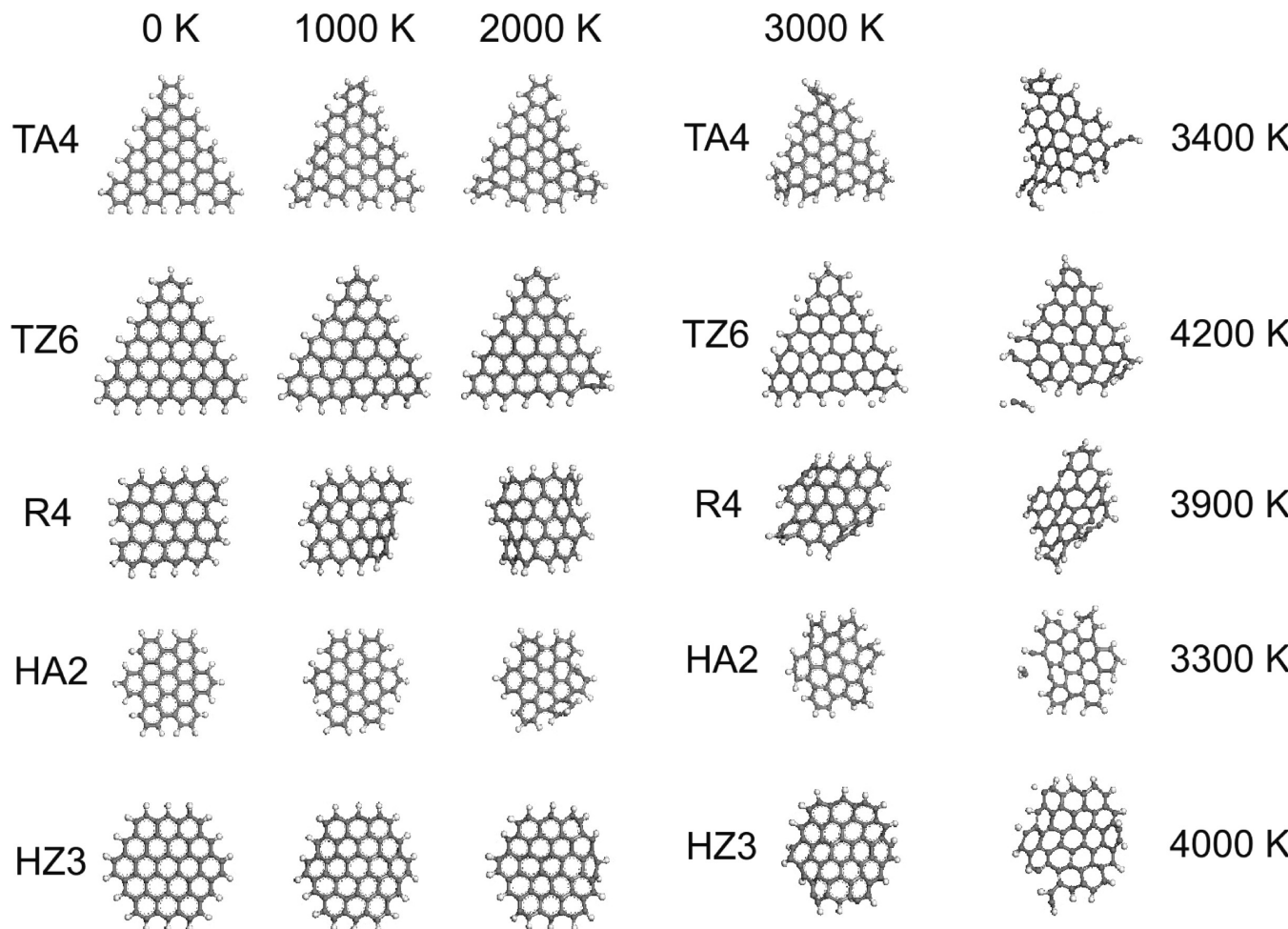


Figure 2. Snapshots of the classical molecular dynamic simulations for a set of GNFs at 20.0 ps of production time and temperatures of 1000 and 2000 K. The $T = 0$ K snapshots show the initial geometries after a classical molecular mechanics optimization.

of nanographene structures can occur by growth from carbon rich plasmas,^{48,49} through the fragmentation of larger graphene sheets. Thus, to develop and improve potential methods to experimentally construct GNFs in a controlled fashion, an estimate of their stability as the temperature increases is very helpful. In order to assess the temperature thresholds for which the carbon–carbon bonding frame starts to be compromised, we have performed classical molecular dynamic simulations described in the previous section. The results of these simulations are presented in Figures 2 and 3. In Figure 2, snapshots corresponding to the last step of production time (20.0 ps) are shown for temperatures of 1000 and 2000 K. The 0 K snapshots are obtained by carrying out a classical geometry optimization on the input structures. As one can see, the planarity of the GNFs is well preserved at 1000 K, and it is approximately retained even at 1500 K. When the temperature increases to 2000 K, however, all nanoflakes display some degree of bending, especially the nanoflakes with armchair borders (TA4, R4, HA2).

For a temperature of 3000 K, the TA4, R4, and HA2 nanoflakes exhibit a high degree of distortion. The R4 nanoflake (chemical formula $C_{48}H_{18}$, $L_A \approx 0.92$ nm, $L_Z \approx 1.11$ nm), with two armchair and two zigzag borders, is the most affected, followed by TA4 ($C_{60}H_{24}$, $L_A \approx 1.70$ nm), with strong bending at its tips. The bond breaking onset occurs at different temperatures depending on the type of GNF. The HA2 ($C_{42}H_{18}$,

Figure 3. Snapshots of the classical molecular dynamics simulations of some GNFs at 20.0 ps for a temperature of 3000 K (left). For very high temperatures, the nanoflakes start to lose their structural stability (covalent bonds breaking, new covalent bonds forming), as one can see by looking at the corresponding final snapshots on the right side.

$L_A \approx 0.57$ nm) and TA4 structures start to degrade under nearly the same conditions, at 3300 and 3400 K, respectively. The rectangular R4 nanoflake, on the other hand, shows its first bond dissociations at a temperature of 3900 K. The GNFs less affected by the increase of temperature are HZ3 ($C_{54}H_{18}$, $L_Z \approx 0.66$ nm) and TZ6 ($C_{61}H_{21}$, $L_Z \approx 1.72$ nm), with critical temperatures of 4000 and 4200 K, in this order. These results lead one to conclude that hydrogen-passivated zigzag borders give more thermal stability to the nanoflakes in contrast with hydrogen-passivated armchair borders. For the sake of comparison, Barnard and Snook²³ performed first-principles molecular dynamics calculations for a set of GNFs (HZ2–HZ6, R3–7) without hydrogen passivation of dangling bonds. Their simulation showed that the HZ2 structure is stable (no bonding breaks) for temperatures up to 2400 K, while the R3 structure starts to degrade for a temperature as low as 1200 K. Such outcomes allowed them to suggest that fragments of nanographene are stable to the nanographene-to-fullerene nanocarbon transition, but very high temperatures can turn these small sheets into amorphous nanocarbon, which is in agreement with the data obtained from our classical molecular dynamics computations. Our results suggest a limit around 1500 K for GNFs to be used in high temperature applications which are shape dependent. This is the case of using GNFs as materials for the development of hot gas sensors to probe the gas emission from automobiles.

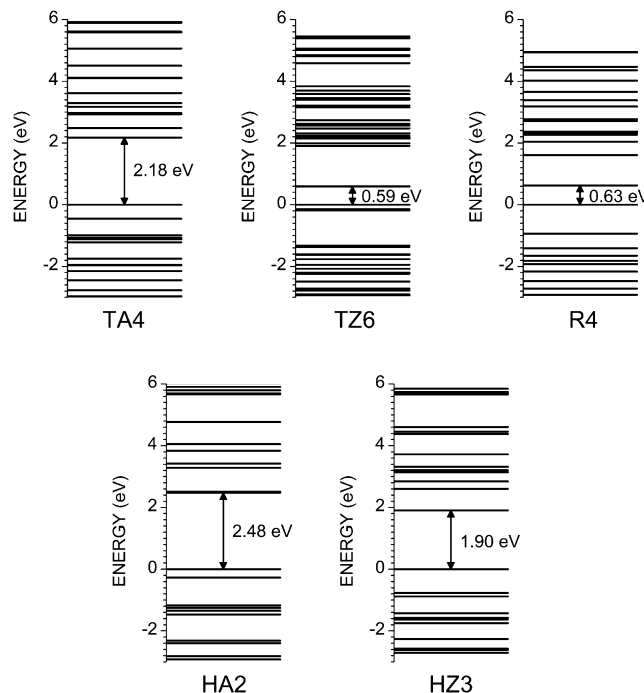


Figure 4. Electronic Kohn–Sham energy levels for some selected graphene nanoflakes in the energy range near the HOMO–LUMO energy gap. The HOMO energy level was adjusted to 0 eV in all graphs. HOMO–LUMO energy gaps are indicated as well.

IV. Nanoflakes for Light Emission and Spintronics

The physical meaning of the Kohn–Sham orbitals has been addressed by several authors.^{50,51} Perdew et al.⁵⁰ obtained that the maximum occupied Kohn–Sham orbital energy (HOMO energy) for an atom of nuclear charge Z is related to its ionization potential and electron affinity. Indeed, it is well established that the HOMO energy predicted by using GGA exchange-correlation functionals is minus half the ionization potential⁵² and that HOMO–LUMO gaps calculated specifically from GGA functionals are relatively accurate.⁵³ Zhan et al.⁵¹ performed a DFT study of several atomic and molecular systems, including organic molecules, using the hybrid exchange-correlation functional B3LYP and the 6-31+G* basis set, showing the existence of a linear correlation between the calculated HOMO (LUMO) energy levels and the ionization potential (electron affinity) obtained experimentally. The HOMO–LUMO energy gaps were observed to be consistently larger (smaller) than experimental first excitation energies (chemical hardness) but also exhibited linear correlation. Taking into account these results, we feel justified in saying that the Kohn–Sham frontier orbitals found after our simulations, albeit unable to give exact values for the real systems, are useful as estimates or as trend indicators. For the sake of comparison, the benzene HOMO and LUMO energies obtained using our methodology were -6.2 and -1.0 eV, giving a HOMO–LUMO energy gap of 5.2 eV, close to the 5.4 eV gap found by Handy and Tozer⁵² using the HCTH exchange-correlation functional (the experimental value of the HOMO \rightarrow LUMO transition energy is 4.9 eV).

Looking to Figure 4, one can see the Kohn–Sham electronic energy eigenvalues near the HOMO–LUMO energy gap for the five selected nanoflakes, TA4, TZ6, R4, HA2, and HZ3. The corresponding HOMO–LUMO energy gaps are also shown. The smallest values for the HOMO–LUMO gap are observed for the TZ6 (0.59 eV) and R4 (0.63 eV) GNFs, which have a

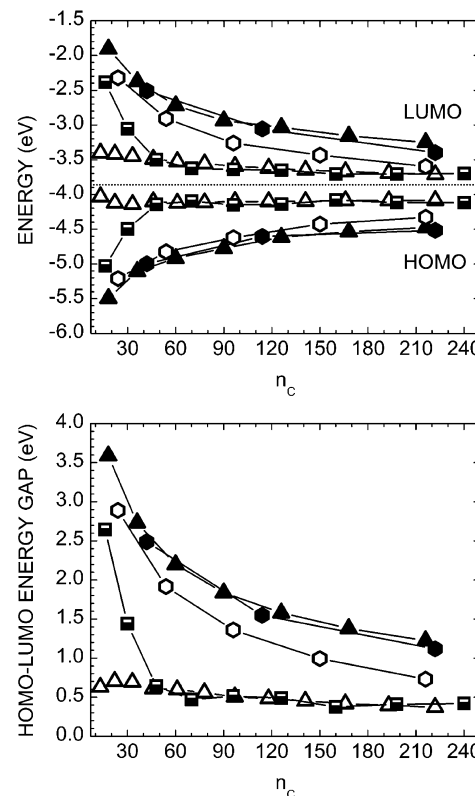


Figure 5. Top: HOMO and LUMO energy levels for the TA (solid triangles), TZ (open triangles), R (black and white squares), HA (solid hexagons), and HZ (open hexagons) GNFs. Bottom: corresponding HOMO–LUMO gaps.

somewhat similar distribution of energy levels. There is also some similarity between the energy level spacings of the two armchair nanoflakes, TA4 and HA2. The HZ3 GNF, on the other hand, has a very distinct distribution of electronic energy levels in comparison with TZ6, with a much larger HOMO–LUMO energy gap of 1.90 eV.

The energy levels for the HOMO and LUMO Kohn–Sham orbitals of several GNFs with different shapes and numbers of carbon atoms (n_c) are shown at the top of Figure 5. One can see that the HOMO (LUMO) energy values tend to increase (decrease) with n_c for all GNFs. The TZ HOMO and LUMO energies, however, have only a small variation as n_c gets larger. The TA and HA HOMO (LUMO) curves are very similar, as well as the R and TZ curves for $n_c > 50$. On the other hand, HZ GNFs present HOMO and LUMO energies between the TA–HA and R–TZ values for the same n_c . Extreme HOMO energy values are -4.0 eV (TZ2, $n_c = 13$), -5.5 eV (TA2, $n_c = 18$), -4.1 eV (R10, $n_c = 240$), and -4.5 eV (TA8, $n_c = 216$). Analogue figures for the LUMO energies are -3.4 eV (TZ2, $n_c = 13$), -1.9 eV (TA2, $n_c = 18$), -3.7 eV (R10, $n_c = 240$), and -3.3 eV (TA8, $n_c = 216$). The LUMO energy for HA4 ($n_c = 222$) was -3.4 eV.

At the bottom of Figure 5, we show the HOMO–LUMO energy gap for the GNFs as a function of n_c . The HOMO–LUMO gap decreases as n_c increases for all GNFs, with the largest variation being observed for the TA GNFs, from 3.59 eV ($n_c = 18$) to 1.23 eV ($n_c = 216$). In comparison, photons of visible light have energies within the 1.6 – 3.3 eV range. The smallest energy variation is observed for TZ GNFs, from 0.63 eV ($n_c = 13$) to 0.37 eV ($n_c = 222$). Differently from the other GNFs, the TZ structures have a small increase in their HOMO–LUMO gap, of about 75 meV, as n_c varies from 13

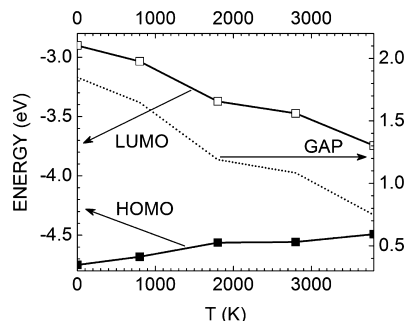


Figure 6. Effect of temperature on the HZ3 GNF frontier orbitals. Solid line, solid squares: HOMO energy. Solid line, open squares: LUMO energy. Dashed line: HOMO–LUMO energy gap.

to 22, caused mainly by a slight decrease of the HOMO energy level (see top of Figure 5). This effect is due to the net spin polarization observed for these nanoflakes, as we will see later, which modifies the electronic structure and cancels the typical gap increase for smaller nanostructures due to quantum confinement effects. For example, the HOMO–LUMO gap obtained by neglecting spin polarization for TZ3 is 2.21 eV, a value much larger than the 0.69 eV observed for the ground state with net spin 3/2. The maximum variations of the HOMO–LUMO energy gaps for R and HZ GNFs are very similar, of about 2.2 eV, with R HOMO–LUMO gaps in the 0.42–2.64 eV energy range and HZ HOMO–LUMO gaps in the 0.73–2.89 eV energy range. The HA HOMO–LUMO gap, on the other hand, varies by about 1.4 eV, decreasing from 2.49 to 1.12 eV.

As we have previously discussed, when the nanoflakes are subjected to increasing temperatures, their structural features may change significantly. Thus, one can argue how these structural changes do affect the HOMO–LUMO energy gaps. To address this issue, we have performed DFT calculations (using the same parameters presented in the beginning of this section) for some representative snapshots of the classical molecular dynamics performed for the HZ3 GNF at temperatures of 800, 1800, 2800, and 3800 K (above 4000 K, the HZ3 GNF loses its structural integrity due to bond dissociation). The HOMO–LUMO energy gaps, as well as the HOMO and LUMO energy levels, for the selected snapshots at a given temperature were averaged, the results being presented in Figure 6. From it, one can see that, as the temperature increases, the HOMO (LUMO) energy levels tend to increase by a few tenths of eV. The LUMO energy level, however, is more affected by the structural deformations induced by temperature, decreasing by almost 1 eV as the temperature is raised from 0 K (which corresponds to the geometry optimized using classical molecular dynamics without temperature effects) to 3800 K. The HOMO–LUMO energy gap decreases as well, from about 1.9 eV (0 K) to about 0.75 eV (3800 K) due to the deviation of the GNF from its 0 K planar configuration (curvature) induced by the temperature increase. At 300 K (room temperature), one can estimate an average HOMO–LUMO energy gap of 1.8 eV for the HZ3 GNFs, 0.1 eV below the 0 K calculated value. It is reasonable to predict that the HOMO–LUMO gap decrease with temperature will also be observed for other GNF types, as the structural changes observed after the classical molecular dynamics simulations are very similar for all shapes.

Considering that quantum dots can be used to produce light-emitting devices,⁵⁴ these results imply the feasibility of using very small flakes of graphene or analogue structures patterned in graphene sheets to produce light emission covering the full visible spectra. In fact, a first-principles study of chemically

modified graphenes with arrays of quantum-dot-like uncoated carbon triangles surrounded by hydrogenated carbon stripes revealed that the band gap of these quantum dot arrays can be tuned, allowing potential light-emitting applications.⁵⁵ To check this possibility for the GNFs under study, we have performed excited state calculations for a set of triangular armchair nanoflakes (TA2–TA6) within the time-dependent DFT formalism (TDDFT) using the NWChem code.^{56,57} However, the quality of a TDDFT calculation is strongly dependent on the exchange-correlation (XC) functional chosen.⁵⁸ Several works have investigated the performance of different XC functionals.^{59–63} Very recently, Jacquemin et al.⁵⁸ performed an extensive TDDFT benchmark to probe the capabilities of TDDFT to describe the singlet-excited states of approximately 500 organic compounds including (bio)organic molecules and dyes. The best functionals in comparison with reference data were the X3LYP, B98, PBE0, and mpW1PW91 functionals, and the long-range-corrected hybrid functional LC- ω PBE(20). In particular, the PBE0 exchange correlation⁶⁴ displayed one of the best overall results, with a mean absolute error of about 0.22 eV over 614 experimental excited states, and with most probable error close to zero.

Taking these results into account, the TA2–TA6 graphene nanoflakes were optimized using the PBE0 functional and a 6-31G(d,p) basis set. Afterward, excited states and oscillator strengths were obtained within the TDDFT framework, from which the UV–vis absorption spectra of the GNFs were obtained. The results of these computations are shown in Figure 7. As one can see from the top part, the UV–vis spectra highest peaks are consistently shifted to larger wavelengths (smaller energies) when N increases. The TA4 GNF should absorb near the beginning of the violet range, at 380 nm, while the TA5 has its main absorption peak at 444 nm (purplish-blue), and the TA GNF exhibits a maximum at 506 nm (green). Plotting the energy values corresponding to the UV–vis absorption maxima (E_{\max}) as a function of N (Figure 7, middle-left), one can see a linear trend that can be fitted approximately by $E_{\max} = 121.41 + 64.402N$ (in nm). Using this linear fit, one can estimate that the TA7 E_{\max} value is 572 nm (greenish-yellow). The same figure for TA8 is 636 nm (red). The relative intensities of the absorption maxima also obey a linear scaling rule with N , as depicted in the middle-right part of Figure 7.

In order to estimate the luminescence peak of the TA nanoflakes, a geometry optimization was performed for the first excited state of the smallest GNF, TA2. This geometry optimization provided us with a Stokes shift estimate of about 11.6 nm, which was applied uniformly to the linear fit for E_{\max} (dotted line in the middle-left of Figure 7). The predicted emission wavelengths for TA5, TA6, and TA8 are 455 nm (A), 519 nm (B), and 648 nm (C), respectively, and are marked on the CIE 1931 chromaticity space diagram shown at the bottom of Figure 7. The gamut triangle formed by these wavelengths covers the most part of the CIE diagram, delimiting the range of accessible colors from all possible combinations of ABC intensities, and includes the white color near its center, reinforcing the potential use of triangular armchair (or other suitable shapes) graphene nanoflakes to build colored and white light-emitting nanodevices.

As the DFT calculations we performed were spin unrestricted, we have also checked the spin polarization of each GNF. For all nanoflakes, except for the TZ ones, the α and β orbital occupations were identical, with no unpaired electrons being observed. In contrast, an interesting pattern was observed for TZ GNFs; namely, a TZ optimized nanoflake has exactly N

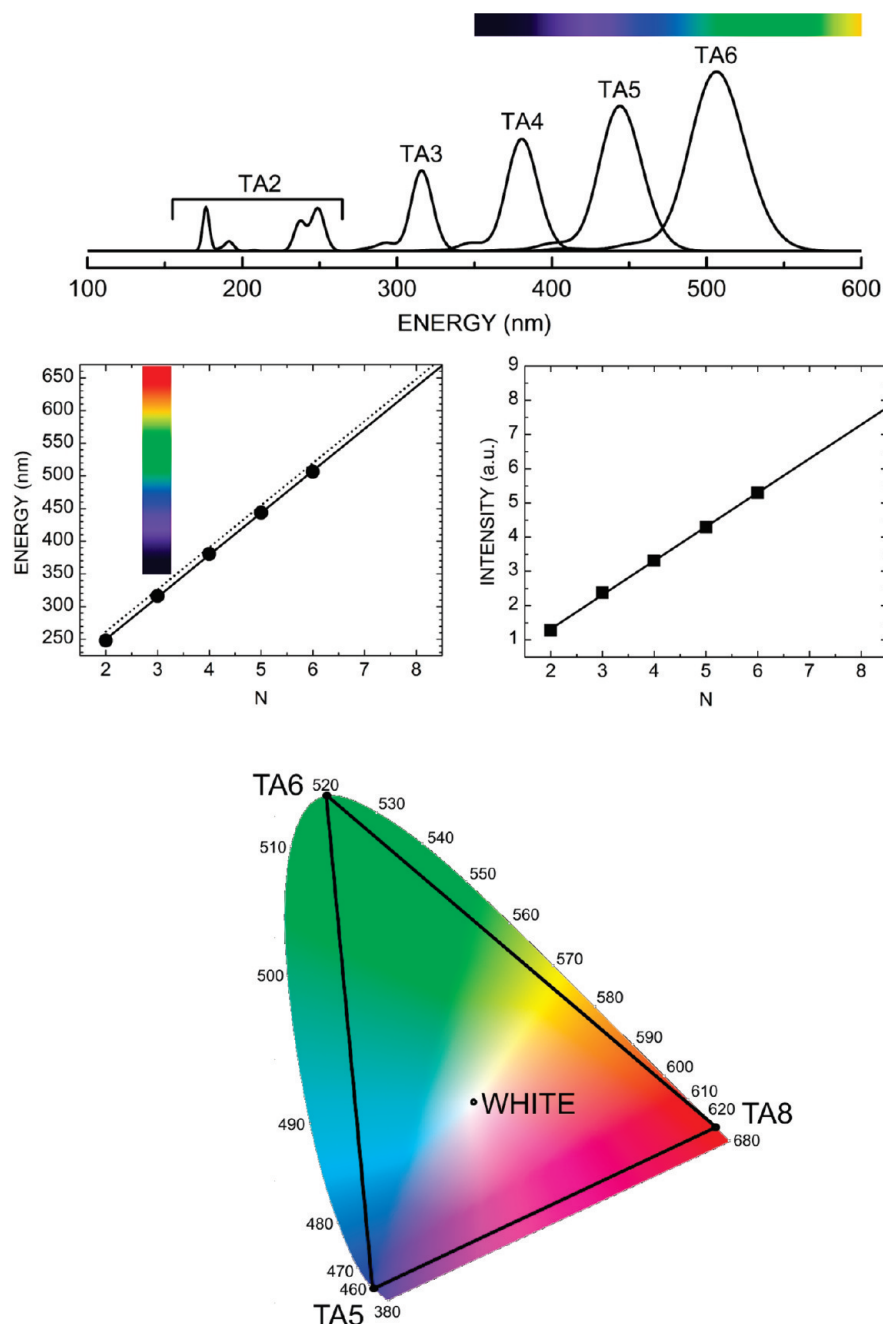


Figure 7. Top: UV-vis absorption spectra for a set of triangular armchair graphene nanoflakes obtained from TDDFT computations. Middle, left: energy plot depicting the first UV-vis absorption maximum as a function of N (solid circles), and respective linear fit (solid line). The dotted line shows the expected energy for the first fluorescence maximum of these GNFs. Middle, right: relative intensity of the first UV-vis absorption peak as a function of N . Bottom: chromaticity diagram (CIE 1931) showing the color gamut one can obtain from the luminescence of three selected TA nanoflakes. Accessible colors are those inside the triangular region and include the white color, as indicated.

α unpaired electrons, being ferromagnetic (FM) even when N is odd, in which case the number of electrons is even. If we switch off the D_{3h} symmetry constraint for the TZ nanoflakes, there are some cases (specifically, for $N = 2, 3, 4, 6, 8, 10, 12, 13$) where a slightly asymmetric shape leads to a slightly smaller value of the total energy, as shown in Table 2 (except for TZ13, which is smaller by 0.67 eV in the asymmetric case). For $N = 5, 7, 9, 11$, the asymmetric TZ GNFs have an electronic structure with identical occupation of α and β orbitals, but they are superseded by the optimized structures preserving the D_{3h} point group symmetry, which have smaller total energy. These symmetric structures have just the electron orbital occupation required to respect the aforesaid pattern of unpaired α electrons. Indeed, all D_{3h} TZ GNFs follow this pattern, except TZ13 that,

opportunely, has a total energy larger than the respective asymmetric GNF. The HOMO-LUMO energy gap, on the other hand, changes significantly if one switches from a symmetric TZG GNF to an asymmetric one when the number of unpaired electrons is different in each case (see the fourth column of Table 2).

Figure 8 shows the spin density and density of states per spin for the TZ2, TZ4, and TZ8 GNFs. The zigzag edges have a strong degree of α -spin polarization. As a matter of fact, it was observed that, for rectangular graphene nanoribbons (RGNs), zigzag edges with at least three consecutive carbon hexagon units are spin polarized for nanoribbon widths larger than 1 nm.⁶⁵ According to first-principles calculations, antiferromagnetic RGNs are energetically preferred.⁶⁶ It is true that DFT spin

TABLE 2: HOMO and LUMO Energy Levels and HOMO–LUMO Gaps for Asymmetric (TZNa) and Symmetric (TZNs) TZ Nanoflakes, as Well as the Number of Unpaired Electrons (UE) for Each GNF and the Difference of Total Energy between TZNa and TZNs (Energy a–s)

GNF	HOMO (eV)	LUMO (eV)	HOMO–LUMO gap (eV)	UE	energy a–s (meV)
TZ1a	−6.216	−1.033	5.183	0	−1.71
TZ1s	−6.218	−1.031	5.187	0	
TZ2a	−4.030	−3.401	0.629	1	−2.06
TZ2s	−4.030	−3.401	0.629	1	
TZ3a	−4.121	−3.417	0.704	2	−3.07
TZ3s	−4.121	−3.417	0.704	2	
TZ4a	−4.141	−3.449	0.692	3	−5.09
TZ4s	−4.141	−3.448	0.693	3	
TZ5a	−3.974	−3.674	0.300	0	238
TZ5s	−4.102	−3.490	0.612	4	
TZ6a	−4.121	−3.524	0.597	5	−9.74
TZ6s	−4.121	−3.523	0.598	5	
TZ7a	−3.982	−3.729	0.253	0	252
TZ7s	−4.117	−3.557	0.560	6	
TZ8a	−4.099	−3.593	0.506	7	−18.7
TZ8s	−4.098	−3.593	0.505	7	
TZ9a	−3.978	−3.772	0.206	0	253
TZ9s	−4.102	−3.620	0.482	8	
TZ10a	−4.098	−3.647	0.451	9	−30.4
TZ10s	−4.096	−3.645	0.451	9	
TZ11a	−3.981	−3.804	0.177	0	245
TZ11s	−4.086	−3.669	0.417	10	
TZ12a	−4.088	−3.692	0.396	11	−44.4
TZ12s	−4.085	−3.690	0.395	11	
TZ13a	−4.083	−3.711	0.372	12	−674
TZ13s	−4.084	−3.824	0.208	0	

unrestricted calculations are usually subjected to spin contamination effects which, however, are small in comparison with unrestricted Hartree–Fock calculations.^{67,68} This allows for a better description of adsorption geometries and binding energies using DFT. The antiferromagnetic or ferromagnetic tendencies of the ground states for polycyclic aromatic hydrocarbons, on the other hand, depend on the choice of the density functional and on the size of the system, which can affect the relative influence of the antiferromagnetic and ferromagnetic states.⁶⁹ Notwithstanding that, our results are clearly in agreement with the work of Wang et al.,²⁸ which have shown, using benzenoid graph theory and first-principles calculations within local spin density approximation (LSDA), that zigzag-edged D_{3h} triangular GNFs have nonzero net spin which increases linearly as a function of the linear size. This spin linear scaling points toward possible applications, such as using nanographene sculpting to control the distribution of spins in a graphene-based spintronic device or even a graphene quantum computer.

Finally, in Figure 9, isosurfaces representing the HOMO and LUMO orbitals of the TA4, TZ6, R4, HA2, and HZ3 GNFs are displayed, together with their respective densities of states. Both the HOMO and LUMO wave functions for the TA4 GNF have e'' symmetry and are 4-fold degenerate (taking the spin into account). The same occurs for the TZ6 GNF (TA4 and TZ6 share the same D_{6h} point group) but with double degeneracy, with the HOMO state being assigned to α spin and the LUMO state to β spin. The HOMO and LUMO orbitals of TA4 have charge densities concentrated along C–C bonds, while, for TZ6, the HOMO and LUMO charge densities are mainly centered at single carbon atoms. The frontier orbitals of the R4 GNF, on the other hand, have b_g (HOMO) and a_u (LUMO) symmetry, being doubly degenerate and with charge densities disposed along C–C bonds. The HA2 and HZ3 GNFs have

both e_{1g} (π) HOMO and e_{2u} (π^*) LUMO orbitals like benzene, each one with 4-fold degeneracy.

V. Shape and Border Related Infrared Fingerprints of Graphene Nanoflakes

The normal modes of vibration and the infrared spectra of the TA4, TZ6, R4, HA2, and HZ3 GNFs were calculated using the Perdew–Burke–Ernzerhof exchange-correlation functional⁷⁰ and the DNP basis set. The accuracy of different GGA functionals/basis sets to describe the vibrational frequencies of 122 molecules was investigated by Merrick et al.⁷¹ Frequencies predicted using the PBE/6-311+G(2df,p) combination, according to that work, must be corrected by a scale factor of 0.9948 in comparison with experimental data. The DNP basis set, on the other hand, is as accurate as the 6-311+G(3df,2pd) Gaussian basis set.^{43,44,72} To ensure a high quality geometry optimization, the thresholds for convergence were tightened up in comparison with the parameters of section II; the total energy variation tolerance in two subsequent optimization steps was set to be smaller than 5×10^{-6} Ha, while the maximum force per atom must be smaller than 5×10^{-4} Ha/Å. The largest atomic displacement allowed was 0.001 Å.

The following symmetries are predicted for the normal modes of vibration: (i) $28a'_1 + 27a'_2 + 110e' + 4a''_1 + 13a''_2 + 54e''$ for TA4, (ii) $27a'_1 + 26a'_2 + 108e' + 10a''_1 + 17a''_2 + 52e''$ for TZ6, (iii) $65a_g + 31b_g + 32a_u + 64b_u$ for R4, (iv) $10a_{1g} + 9a_{2g} + 3b_{1g} + 7b_{2g} + 18e_{1g} + 40e_{2g} + 3a_{1u} + 6a_{2u} + 10b_{1u} + 10b_{2u} + 38e_{1u} + 20e_{2u}$ for HA2, and (v) $12a_{1g} + 11a_{2g} + 4b_{1g} + 8b_{2g} + 22e_{1g} + 48e_{2g} + 4a_{1u} + 7a_{2u} + 12b_{1u} + 12b_{2u} + 46e_{1u} + 24e_{2u}$ for HZ3. After completing the vibrational analysis, we have found imaginary frequencies only for the TA4 nanoflake. These imaginary frequencies were (in units of cm^{−1}) 76.3*i* (mode 1), 74.2*i* (modes 2 and 3), 24.3*i* (modes 4 and 5), and 2.6*i* (mode 6). It is known, however, that DFT implementations have limitations in their numerical integration methodologies which usually lead to imaginary vibrational frequencies with magnitude smaller than 100 wavenumbers,^{73–75} so we have not refined further the geometry optimization of the TA4 GNF.

Selection rules constrain the number of active infrared modes for a symmetric molecule. In the case of the six GNFs we studied, the numerical analysis of the results produced the following sets of modes with infrared intensity different from zero: (i) $108e' + 13a''_2$ for TA4, (ii) $2a'_1 + 100e' + 17a''_2 + 4e''$ for TZ6, (iii) $32a_u + 64b_u$ for R4, (iv) $6a_{2u} + 38e_{1u}$ for HA2, and (v) $7a_{2u} + 46e_{1u}$ for HZ3. Figure 10 shows the infrared spectra of the GNFs in the wavenumber range varying from 0 to 3300 cm^{−1}. In order to contrast their main features, it is interesting to divide the wavenumber full range into three subintervals: A (0–1000 cm^{−1}), B (1000–1800 cm^{−1}), and C (3000–3300 cm^{−1}). The 2800–3000 cm^{−1} subinterval does not contain any peaks, as expected from polycyclic aromatic hydrocarbons (PAHs).⁷⁶ It is worth mentioning that infrared emission from PAHs in astronomical objects has been widely investigated by astrochemists.⁷⁶

Figure 11 shows the infrared spectra in the A range. One can note that there are two peak structures approximately in the same wavenumber region, between 840 and 915 cm^{−1} (see the peaks inside the dashed rectangles), for the TZ6 and HZ3 spectra. These peaks are assigned to vibrations corresponding to the bending out-of-plane of C–H groups (CH_{oop}) at the borders of the GNFs. For HZ3, the highest IR absorption in this region is assigned to a normal mode at 901.8 cm^{−1}, with a_{2u} symmetry, while the TZ6 GNF has three pronounced absorption peaks at 845.4, 877.9, and 894.5 cm^{−1}, each one

SPIN DENSITY

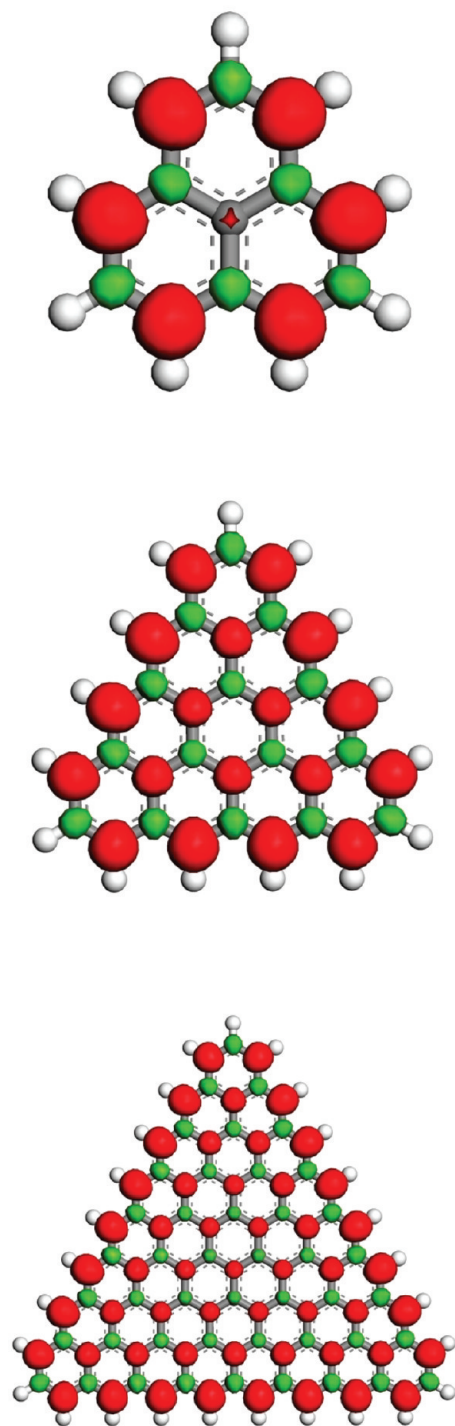


Figure 8. Spin density and DOS for some TZ nanoflakes. Isosurfaces corresponding to 0.015 atomic units of spin. Red (darker) isosurfaces: α spin polarization. Green (lighter) isosurfaces: β spin polarization.

related to vibrations of d_2'' symmetry. The armchair nanoflakes (TA4 and HA2), on the other hand, have infrared absorption bands in the $680\text{--}840\text{ cm}^{-1}$ wavenumber region (peaks inside the dotted rectangles), also related to CH_{oop} vibrations. For HA2, a strong peak occurs at 757.3 cm^{-1} , being related to an a_{2u} vibration, and with two small neighbor peaks at 701.6 cm^{-1} (e_{1u}) and 815.4 cm^{-1} (a_{2u}). The TA4 GNF has three main infrared absorption lines due to d_2'' normal modes at 727.1 , 752.9 ,

and 795.7 cm^{-1} . In comparison with the “pure” zigzag and armchair GNFs, the R4 nanoflake has a wider absorption band (region inside the dash-dotted rectangle) due to CH_{oop} vibrations, ranging from 680 to 900 cm^{-1} . Such a feature is probably due to the presence of both zigzag and armchair borders. The strongest absorption peak occurs at 855 cm^{-1} due to an a_u normal mode. Other traits common to the GNFs with zigzag borders are the CH_{oop} absorption peaks indicated as p_1 (HZ3,

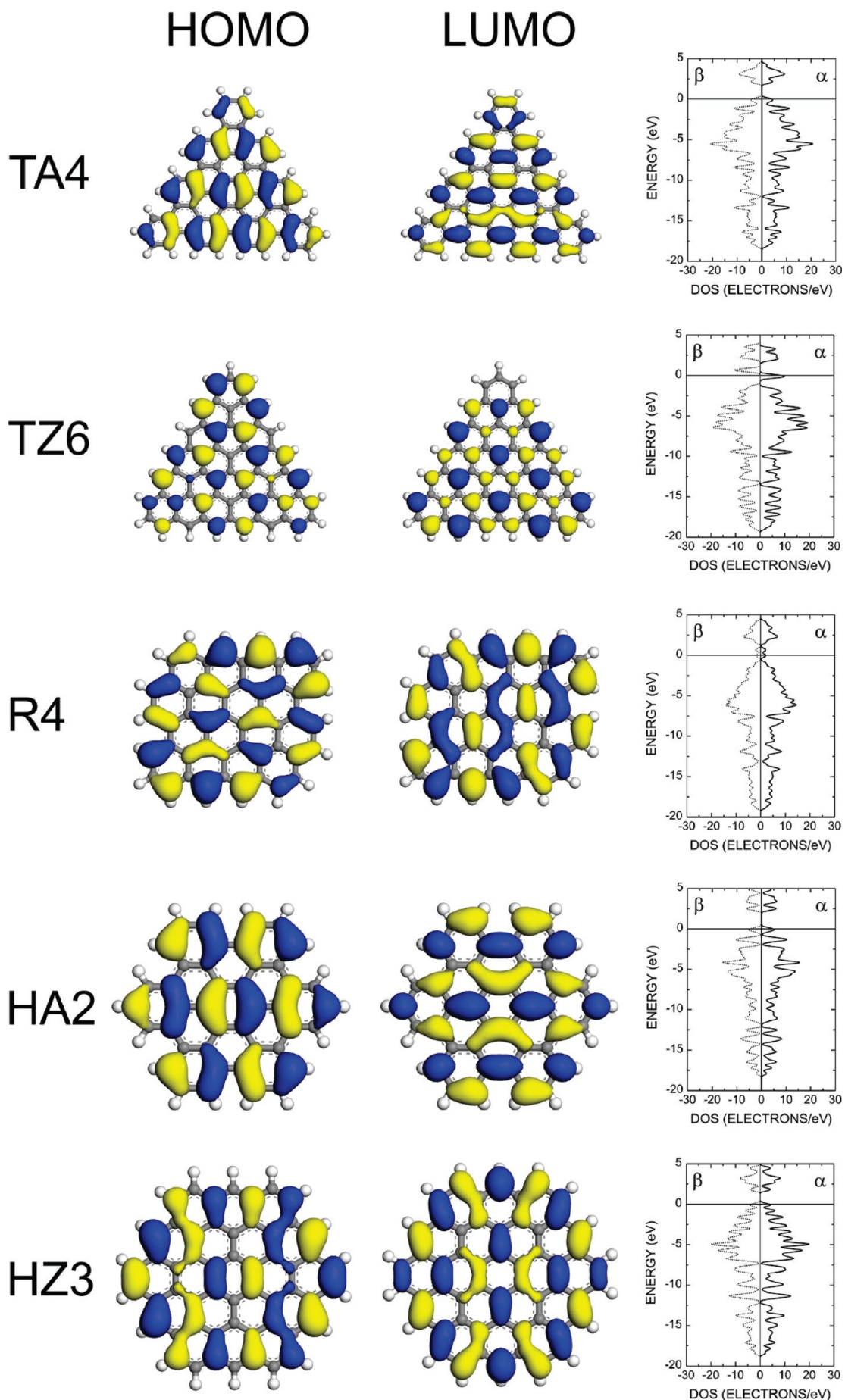


Figure 9. HOMO and LUMO orbitals and DOS for some GNFs.

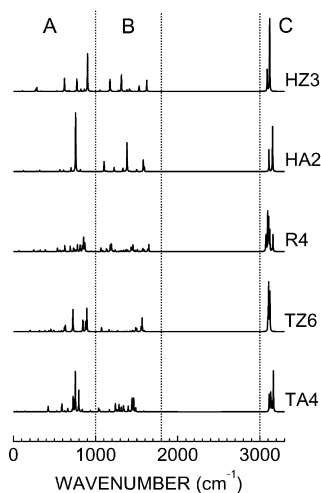


Figure 10. IR spectra of six GNFs. Regions A, B, and C are shown.

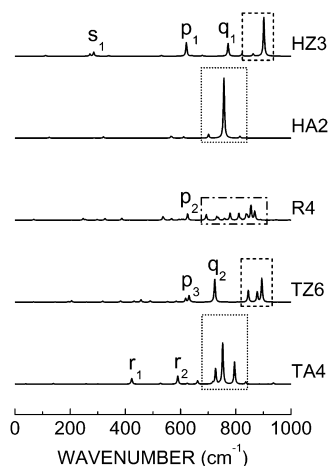


Figure 11. IR spectra of six GNFs for the A (0–1000 cm^{-1}) wavenumber range.

a_{2u}), p_2 ($R4, a_u$, mainly vibrations at the zigzag border), and p_3 ($TZ6, a''_2$), all occurring at approximately 620 cm^{-1} . The HZ3 and TZ6 GNFs also have two similar peaks, identified in Figure 11 as q_1 ($772.3 \text{ cm}^{-1}, a_{2u}$) and q_2 ($724 \text{ cm}^{-1}, a''_2$), involving CH_{oop} vibration patterns with CH groups vibrating in an alternate fashion. The TA4 nanoflake has two characteristic peaks r_1 and r_2 at 424 cm^{-1} ($a''_2, \text{CH}_{\text{oop}}$) and 590.1 cm^{-1} (e'), respectively, the latter one being distinguished by the in-plane bending movement of C–C bonds at the borders. Lastly, we have the s_1 peaks characteristic of HZ3 near 280 cm^{-1} , which may be described as a mixing of in-plane bending and twisting of almost all C–C bonds of the carbon nanostructure.

Looking now to Figure 12, one can see the infrared spectra of the GNFs in the B range. As in the previous paragraph, we search for similarities and differences between the absorption bands possibly related to the type of border (zigzag or armchair) and type of shape. Looking to the spectra inside the dashed rectangles for the HZ3, HA2, R4, and TZ6 GNFs, we note a common pattern formed by one or more smaller peaks, a gap, and one or more higher peaks. For HZ3, HA2, and TZ6, this pattern occurs at approximately the same wavenumber range, between 1470 and 1650 cm^{-1} . In comparison, the corresponding band for R4 is shifted to higher wavenumbers, being between 1540 and 1700 cm^{-1} . The vibrations in these regions are mainly due to the stretching of some C–C bonds and the in-plane bending of C–H bonds. The most relevant peaks (in units of

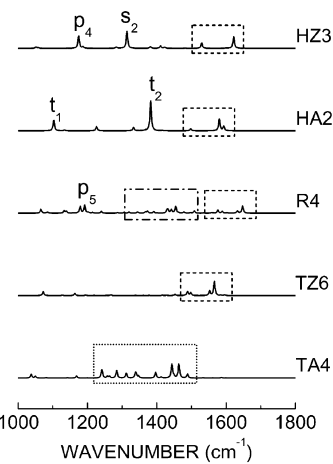


Figure 12. IR spectra of six GNFs for the B (1000–1800 cm^{-1}) wavenumber range.

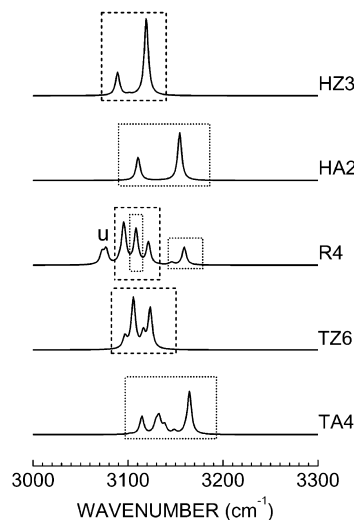


Figure 13. IR spectra of six GNFs for the C (3000–3300 cm^{-1}) wavenumber range.

cm^{-1}) are at 1529.8 and 1622.2 (both e_{1u}) for HZ3; 1498.1 (e_{1u}), 1580.4 (e_{1u}), and 1593.4 (e_{2g}) for HA2; 1489 , 1552.5 , and 1566.2 (all e') for TZ6; and 1576.4 and 1647.8 (both b_u) for R4. The TA4 nanoflake, on the other hand, has as a unique feature a wide band of peaks in the 1220 – 1510 cm^{-1} range (see region inside the dotted rectangle) which also involve C–C stretching and C–H in-plane bending. The most important peaks occur at 1443.8 cm^{-1} (e') and 1464 cm^{-1} (e'). The R4 GNF also has a fingerprint band in the 1310 – 1520 cm^{-1} range, with the highest peaks at 1432 and 1454.7 cm^{-1} , both related to normal modes of b_u symmetry. The p_4 and p_5 peaks in the HZ3 and R4 spectra, respectively, occur at nearly the same wavenumbers, around 1180 cm^{-1} , and are related to a scissor-like movement of $\text{H}-\text{C}=\text{C}-\text{H}$ groups along the edges. The HA2 nanoflake exhibits two fingerprint peaks due to e_{1u} vibrations, t_1 and t_2 , at 1103 and 1382.4 cm^{-1} , respectively. The t_1 vibration may be described as a breathing of the benzene-like rings making up the armchair borders, while the t_2 vibration originates from the stretching of C–C bonds and bending of C–H bonds. Ending the analysis of the B range, we find the s_2 peak of the HZ3 GNF, at 1314 cm^{-1} and due to a mode with e_{1u} symmetry.

The infrared absorption bands above 3000 cm^{-1} (C region) were plotted in Figure 13 and are mainly due to C–H stretching vibrations. Comparing the peaks for HZ3 and HA2 (inside the dashed and dotted rectangles, in this order), we note a similar

structure (small peak, high peak) with minor differences. The two pronounced infrared peaks of HA2 (at 3110.7 and 3154.5 cm^{-1} , both e_{1u}) are shifted to higher wavenumbers and are more apart in comparison with the corresponding peaks of the HZ3 GNF (at 3089.1 cm^{-1} , e_{2g} , and 3119.3 cm^{-1} , e_{1u}). The bands inside the dashed rectangles for HZ3, R4, and TZ6 occur at approximately the same wavenumber interval, 3070–3140 cm^{-1} , and the two highest peaks of each band originate from similar C–H stretching vibrations along the zigzag edges. The peaks inside the dotted rectangles of the R4 infrared spectrum, however, include C–H stretching vibrations along the armchair borders, and are analogues of the two more intense absorption peaks of the HA2 nanoflake. The R4 GNF also has a unique set of two peaks at u , corresponding to vibrations with wavenumbers 3072.7 and 3077 cm^{-1} , both with b_u symmetry. Contrasting the TZ6 and TA4 spectra, we see some similarities with the behavior observed for HZ3 and HA2, where the armchair structure peaks are shifted to higher wavenumbers and more apart in comparison with the respective zigzag structures.

It is worthwhile to consider how temperature modifies the infrared spectra of graphene nanoribbons studied here (after all the classical molecular dynamics results we have presented here). Indeed, there is a single experimental study depicting the temperature dependence of the infrared absorption spectra of free polycyclic aromatic hydrocarbons (PAHs).⁷⁷ In this study, results of measurements of IR absorption bands of gas-phase PAHs at temperatures up to about 1000 K were presented, and it was shown that the band positions depend on the vibrational content of the molecules through anharmonic couplings. In general, the bands tend to be shifted to lower wavenumbers as the temperature increases. For example, for coronene (which corresponds to the HZ2 GNF), the absorption band at 3100 cm^{-1} is shifted by about -100 cm^{-1} as the temperature approaches 1200 K. A smaller red shift (of about -10 cm^{-1}) was observed for the absorption bands near 850 cm^{-1} . Making an extrapolation for the GNFs we have investigated, one can hope that increasing temperatures will promote a red shift of the IR absorption bands which is more pronounced for the bands with highest wavenumbers, but preserving the observed molecular signatures.

VI. Conclusions

In summary, we have used classical molecular dynamics and density functional theory first-principles calculations to investigate small graphene nanoflakes with triangular, rectangular, and hexagonal shapes, and zigzag and armchair borders. The CMD computations were performed to optimize the geometries of a set of representative nanoflakes (TA4, TZ6, R4, HA2, HZ3) with dangling bonds passivated by hydrogen atoms and, afterward, to study the stability of these nanostructures under different temperatures using a forcefield able to reproduce the process of formation and breaking of chemical bonds. We observed that the GNFs preserve their planarity for temperatures of up to 1000 K, and suffer severe distortion and bond dissociation for temperatures above 3000 K and production time of 20.0 ps, tending to form amorphous carbon nanostructures. The armchair GNFs, HA2 and TA4, are less stable, starting to degrade at 3300 and 3400 K, respectively. Zigzag structures (TZ6 and HZ3) are more stable in comparison, exhibiting bond breaking for temperatures of 4000 K or more. The rectangular R4 GNF, having both armchair and zigzag borders, has intermediate stability, with critical temperature for bond dissociation of 3900 K.

The DFT electronic structure of the graphene nanoflakes revealed that the behavior of the HOMO–LUMO energy gaps

as a function of the number of carbon atoms, n_C , is very sensitive to the shape and type of GNF border. Triangular armchair and hexagonal armchair GNFs have a very similar behavior of the HOMO–LUMO gap as n_C increases, with the triangular armchair nanoflakes displaying the largest gap variation, from 3.59 eV ($n_C = 18$) to 1.23 eV ($n_C = 216$). The triangular zigzag GNF has a small HOMO–LUMO gap variation with n_C , ranging from 0.63 eV ($n_C = 13$) to 0.37 eV ($n_C = 222$). The hexagonal zigzag nanoflake has, for a given value of n_C , a HOMO–LUMO gap with value intermediate between those of the armchair nanoflakes and the triangular zigzag ones. The rectangular nanoflakes, for $n_C > 60$, follow closely the HOMO–LUMO gap curve of the triangular zigzag GNFs. As the temperature increases, structural deformations of the HZ3 nanoflakes tend to decrease their HOMO–LUMO gaps, a behavior that can be expected for the other GNFs as well. After performing TDDFT calculations to obtain the UV–vis absorption spectra of TA2–6 GNFs, we confirmed the potential of using small GNFs to build optical emission nanodevices covering the full range of the visible spectrum. In particular, the UV–vis maximum absorption energies and intensities scale linearly with the linear size of the GNF. Analysis of the spin state of the GNFs, on the other hand, revealed that only the triangular zigzag nanoflakes have an excess of α electrons, being ferromagnetic, and that the number of unpaired α spins increases linearly with the linear size. This result, however, depends on a delicate equilibrium between symmetric and almost symmetric optimized structures; namely, when the optimized almost symmetric structure has a total energy smaller than the corresponding symmetric one, both will have in general the same spin state; otherwise, when the symmetric structure has a total energy smaller than the asymmetric one, the symmetric structure will have exactly the spin required to fulfill the spin linear scaling rule, while the optimized asymmetric nanoflake will have zero total spin. These results reinforce the potential of zigzag triangular graphene nanoflakes, or analogous nanostructures, for spintronic applications.

For the six GNFs investigated using CMD techniques, we have performed a very tight DFT geometry optimization to obtain their normal modes of vibration and infrared spectra. Mode assignments were carried out, and a series of fingerprints related with the type of border and shape were observed. For example, there are similarities between bands of the infrared spectra of zigzag nanoflakes in the 840–915, 1470–1650, and 3070–3140 cm^{-1} ranges. The R4 GNF has absorption bands in common with the zigzag nanoflakes in the wavenumber ranges 1540–1700 and 3080–3130 cm^{-1} and two peaks at about 3110 and 3160 cm^{-1} corresponding to vibrations mainly along the armchair sides that have analogue peaks in the infrared absorption of the HA2 and TA4 armchair GNFs. TA4 has two fingerprints, r_1 and r_2 , at 424 and 590.1 cm^{-1} , respectively, and a wide band of peaks in the 1220–1510 cm^{-1} range. The HZ4 nanoflake has peak fingerprints at s_1 (near 280 cm^{-1}) and s_2 (1314 cm^{-1}), while the HA2 nanoflake has molecular signatures at t_1 and t_2 , corresponding to the wavenumbers 1103 and 1382.4 cm^{-1} , in this order. The R4 GNF, on the other hand, has two characteristic peaks at u , between 3070 and 3080 cm^{-1} . In the 3000–3300 cm^{-1} wavenumber interval, the infrared absorption peaks of the armchair structures are shifted to higher wavenumbers and are more apart in comparison with the corresponding peaks of the zigzag nanoflakes. These molecular signatures can be helpful in the experimental identification of small GNFs even when temperature effects are taken into account, as such effects probably lead only to absorption band red shifts.

Finally, we must note that the GNFs we have studied in this work are very small in comparison with nanoflakes obtained experimentally. As a matter of fact, graphene nanoflakes with average diameters of approximately 30 nm and edges decorated with carboxylic acid groups were prepared through a chemical treatment of single-wall carbon nanotubes, with a small number of internal defects,⁷⁸ while femtosecond laser ablation of graphite was shown to produce small nanoflakes with a few tens of nm of diameter.⁷⁹ The anisotropic etching of single layer graphene using activated nickel nanoparticles was also able to produce nanoflakes with characteristic dimensions smaller than 100 nm.¹⁰ In comparison, the largest nanoflake investigated through DFT calculations here is the R10 one ($C_{240}H_{42}$), which has its largest edge measuring only 2.6 nm. Thus, we must take some care to extend the results presented here to GNFs that are at least 1 order of magnitude larger. With respect to the electronic structure, however, we can expect that the HOMO–LUMO gap of a GNF will decrease as its size increases, converging asymptotically to the graphene 0 eV band gap. As for the infrared spectra, we have performed additional calculations for a 4.6 nm GNF (HZ10, $C_{600}H_{60}$) and a 4.2 nm GNF (HZ9, $C_{480}H_{54}$) using the Brenner classical forcefield and the Gasteiger charging. The following features were observed: for wavenumbers smaller than 800 cm^{-1} and larger than 3000 cm^{-1} , a small red shift occurs when one switches from the smallest GNF to the largest one, while bands with wavenumbers between 800 and 2000 cm^{-1} seem to be slightly (a few cm^{-1}) shifted sometimes to higher and sometimes to lower wavenumbers, a trend that possibly will be observed even for GNFs with thousands of atoms. It is also reasonable to assume that nanoflakes larger than 10 nm will exhibit a greater probability of forming internal defects (as shown in ref 78), which will certainly modify the bond dissociation dynamics when these nanostructures are subjected to very high temperatures, a situation we have not taken into account in this work.

Acknowledgment. E.L.A and V.N.F. are senior researchers from the Brazilian National Research Council CNPq and would like to acknowledge the financial support received during the development of this work from the Brazilian Research Agencies CAPES - PROCAD and Rede NanoBioTec, CNPq - INCT-Nano(Bio)Simes, Project No. 573925/2008-9, and FAPERJ/CNPq (Pronex). E.W.S.C. received financial support from CNPq-process number 304338/2007-9 and CNPq-process number 482051/2007-8. A.M.S. and M.S.P. received fellowships from CNPq during the development of this work.

References and Notes

- (1) Katsnelson, M. I. *Mater. Today* **2007**, *10*, 20.
- (2) Novoselov, K. S.; Jiang, D.; Schedin, F.; Booth, T. J.; Khotkevich, V. V.; Morozov, S. V.; Geim, A. K. *Proc. Natl. Acad. Sci. U.S.A.* **2005**, *102*, 10451.
- (3) Geim, A. K.; Novoselov, K. S. *Nat. Mater.* **2007**, *6*, 183.
- (4) Nakada, K.; Fujita, M.; Dresselhaus, G.; Dresselhaus, M. S. *Phys. Rev. B* **1996**, *54*, 17954.
- (5) Ritter, K. A.; Lyding, J. W. *Nat. Mater.* **2009**, *8*, 235.
- (6) Novoselov, K. S.; Geim, A. K.; Morozov, S. V.; Jiang, D.; Zhang, Y.; Dubonos, S. V.; Grigorieva, I. V.; Firsov, A. A. *Science* **2004**, *306*, 666.
- (7) Berger, C.; Song, Z.; Li, X.; Wu, X.; Brown, N.; Naud, C.; Mayou, D.; Li, T.; Hass, J.; Marchenkov, A. N.; Conrad, E. H.; First, P. N.; de Heer, W. A. *Science* **2006**, *312*, 1191.
- (8) Li, X.; Wang, X.; Zhang, L.; Lee, S.; Dai, H. *Science* **2008**, *319*, 1229.
- (9) Stampfer, C.; Güttinger, J.; Hellmüller, S.; Molitor, F.; Ensslin, K.; Ihn, T. *Phys. Rev. Lett.* **2009**, *102*, 056403.
- (10) Campos, L. C.; Manfrinato, V. R.; Sanchez-Yamagishi, J. D.; Kong, J.; Jarillo-Herrero, P. *Nano Lett.* **2009**, *9*, 2600.
- (11) Wang, Z. F.; Shi, Q. W.; Li, Q.; Wang, X.; Hou, J. G.; Zheng, H.; Yao, Y.; Chen, J. *J. Appl. Phys. Lett.* **2007**, *91*, 053109.
- (12) Guo, G.-P.; Lin, Z.-R.; Tu, T.; Gao, G.; Li, X.-P.; Guo, G.-C. *New J. Phys.* **2009**, *11*, 123005.
- (13) Barone, V.; Hod, O.; Scuseria, G. E. *Nano Lett.* **2006**, *6*, 2748.
- (14) Li, D.; Kaner, R. B. *Science* **2008**, *320*, 1170.
- (15) Zhang, Z. Z.; Chang, K.; Peeters, F. M. *Phys. Rev. B* **2008**, *77*, 235411.
- (16) Bahamon, D. A.; Pereira, A. L. C.; Schulz, P. A. *Phys. Rev. B* **2009**, *79*, 125414.
- (17) Bonelli, F.; Manini, N.; Cadelano, E.; Colombo, L. *Eur. Phys. J. B* **2009**, *70*, 449.
- (18) Ezawa, M. *Physica E* **2008**, *40*, 1421.
- (19) Heiskanen, H. P.; Manninen, M.; Akola, J. *New J. Phys.* **2008**, *10*, 103015.
- (20) De Raedt, H.; Katsnelson, M. I. *JETP Lett.* **2008**, *88*, 607.
- (21) Akola, J.; Heiskanen, H. P.; Manninen, M. *Phys. Rev. B* **2008**, *77*, 193410.
- (22) Manninen, M.; Heiskanen, H. P.; Akola, J. *Eur. Phys. J. D* **2009**, *52*, 143.
- (23) Barnard, A. S.; Snook, I. K. *J. Chem. Phys.* **2008**, *128*, 094707.
- (24) Sahin, H.; Senger, R. T. *Phys. Rev. B* **2008**, *78*, 205423.
- (25) Zheng, H.; Duley, W. *Phys. Rev. B* **2008**, *78*, 045421.
- (26) Nagai, H.; Nakano, M.; Yoneda, K.; Fukui, H.; Minami, T.; Bonness, S.; Kishi, R.; Takahashi, H.; Kubo, T.; Kamada, K.; Ohta, K.; Champagne, B.; Botek, E. *Chem. Phys. Lett.* **2009**, *477*, 355.
- (27) Yoneda, K.; Nakano, M.; Kishi, R.; Takahashi, H.; Shimizu, A.; Kubo, T.; Kamada, K.; Ohta, K.; Champagne, B.; Botek, E. *Chem. Phys. Lett.* **2009**, *480*, 278.
- (28) Wang, W. L.; Meng, S.; Kaxiras, E. *Nano Lett.* **2008**, *8*, 241.
- (29) Yazyev, O. V.; Lang, W. L.; Meng, S.; Kaxiras, E. *Nano Lett.* **2008**, *8*, 766.
- (30) Wang, W. L.; Yazyev, O. V.; Meng, S.; Kaxiras, E. *Phys. Rev. Lett.* **2009**, *102*, 157201.
- (31) Schnez, S.; Ensslin, K.; Sigrist, M.; Ihn, T. *Phys. Rev. B* **2008**, *78*, 195427.
- (32) Tang, C.; Yan, W.; Zheng, Y.; Li, G.; Li, L. *Nanotechnology* **2008**, *19*, 435401.
- (33) Libisch, F.; Stampfer, C.; Burgdörfer, J. *Phys. Rev. B* **2009**, *79*, 115423.
- (34) Moradian, R.; Zereshki, P.; Haseli, S.; Hayati, M. *Physica E* **2009**, *41*, 801.
- (35) Romanovsky, I.; Yannouleas, C.; Landman, U. *Phys. Rev. B* **2009**, *79*, 075311.
- (36) Shang, N. G.; Papakonstantinou, P.; McMullan, M.; Chu, M.; Stamboulis, A.; Potenza, A.; Dhesi, S. S.; Marchetto, H. *Adv. Funct. Mater.* **2008**, *18*, 3506.
- (37) Vadukumpilly, S.; Paul, J.; Valiyaveettil, S. *Carbon* **2009**, *47*, 3288.
- (38) Ponomarenko, L. A.; Schedin, F.; Katsnelson, M. I.; Yang, R.; Hill, E. W.; Novoselov, K. S.; Geim, A. K. *Science* **2008**, *320*, 356.
- (39) Tapaszó, L.; Dobrik, G.; Lambin, P.; Biró, L. P. *Nat. Nanotechnol.* **2008**, *3*, 397.
- (40) Wright, N. G.; Horsfall, A. B. *J. Phys. D.: Appl. Phys.* **2007**, *40*, 6345.
- (41) Brenner, D. W.; Shenderova, O. A.; Harrison, J. A.; Stuart, S. J.; Ni, B.; Sinnott, S. B. *J. Phys.: Condens. Matter* **2002**, *14*, 783.
- (42) Ni, B.; Lee, K.-H.; Sinnott, S. B. *J. Phys.: Condens. Matter* **2004**, *16*, 7261.
- (43) Delley, B. *J. Chem. Phys.* **1990**, *92*, 508.
- (44) Delley, B. *J. Chem. Phys.* **2000**, *113*, 7756.
- (45) Perdew, J. P.; Wang, Y. *Phys. Rev. B* **1992**, *45*, 13244.
- (46) Inada, Y.; Orita, H. *J. Comput. Chem.* **2008**, *29*, 225.
- (47) Barnard, A. S.; Russo, S. P.; Snook, I. K. *J. Comput. Theor. Nanosci.* **2005**, *2*, 180.
- (48) Helveg, S.; Lopez-Cartes, C.; Sehested, J.; Hansen, P. L.; Clausen, B. S.; Rostrup-Nielsen, J. R.; Abild-Pedersen, F.; Norskov, J. K. *Nature* **2004**, *427*, 426.
- (49) Raty, J.-Y.; Gygi, F.; Galli, G. *Phys. Rev. Lett.* **2005**, *95*, 096103.
- (50) Perdew, J. P.; Parr, R. G.; Levy, M.; Balduz, J. L., Jr. *Phys. Rev. Lett.* **1982**, *49*, 1691.
- (51) Zhan, C.-G.; Nichols, J. A.; Dixon, D. A. *J. Phys. Chem. A* **2003**, *107*, 4184, and references therein.
- (52) Handy, N. C.; Tozer, D. J. *J. Comput. Chem.* **1998**, *20*, 106, and references therein. .
- (53) Zhang, G.; Musgrave, C. B. *J. Phys. Chem. A* **2007**, *111*, 1554.
- (54) Li, Y.; Rizzo, A.; Mazzeo, M.; Carbone, L.; Manna, L.; Cingolani, R. *J. Appl. Phys.* **2005**, *97*, 113501.
- (55) Wu, M.; Wu, X.; Gao, Y.; Zeng, X. C. *J. Phys. Chem. C* **2010**, *114*, 139.
- (56) Straatsma, T. P.; Aprà, E.; Windus, T. L.; Bylaska, E. J.; de Jong, W.; Hirata, S.; Valiev, M.; Hackler, M.; Pollack, L.; Harrison, R.; Dupuis, M.; Simth, D. M. A.; Nieplocha, J.; Tipparaju, V.; Krishnan, M.; Auer, A. A.; Brown, E.; Cisneros, G.; Fann, G.; Fröhlich, H.; Garza, J.; Hirao, K.;

- Kendall, R.; Nichols, J.; Tsemekhman, K.; Wolinski, K.; Anchell, J.; Bernholdt, D.; Borowski, P.; Clark, T.; Clerc, D.; Dachselt, H.; Deegan, M.; Dyall, K.; Elwood, D.; Glendening, E.; Gutowski, M.; Hess, A.; Jaffe, J.; Johnson, B.; Ju, J.; Kobayashi, R.; Kutteh, R.; Lin, Z.; Littlefield, R.; Long, X.; Meng, B.; Nakajima, T.; Niu, S.; Rosing, M.; Sandrone, G.; Stave, M.; Taylor, H.; Thomas, G.; van Lenthe, J.; Wong, A.; Zhang, Z. *NWChem, A Computational Chemistry Package for Parallel Computers*, version 4.6; Pacific Northwest National Laboratory: Richland, WA, 2004.
- (57) Kendall, R. A.; Aprà, E.; Bernholdt, D. E.; Bylaska, E. J.; Dupuis, M.; Fann, G. I.; Harrison, R. J.; Ju, J.; Nichols, J. A.; Nieplocha, J.; Straatsma, T. P.; Windus, T. L.; Wong, A. T. *Comput. Phys. Commun.* **2000**, *128*, 260.
- (58) Jacquemin, D.; Wathélet, V.; Perpète, E. A.; Adamo, C. *J. Chem. Theory Comput.* **2009**, *5*, 5420.
- (59) Dierksen, M.; Grimme, S. *J. Chem. Phys.* **2004**, *120*, 3544.
- (60) Peach, M. J. G.; Benfield, P.; Helgaker, T.; Tozer, D. J. *J. Chem. Phys.* **2008**, *128*, 044118.
- (61) Silva-Junior, M. R.; Schreiber, M.; Sauer, S. P. A.; Thiel, W. *J. Chem. Phys.* **2008**, *129*, 104103.
- (62) Jacquemin, D.; Perpète, E. A.; Scuseria, G. E.; Ciofini, I.; Adamo, C. *J. Chem. Theory Comput.* **2008**, *4*, 123.
- (63) Jacquemin, D.; Perpète, E. A.; Vydrov, O. A.; Scuseria, G. E.; Adamo, C. *J. Chem. Phys.* **2007**, *127*, 094102.
- (64) Adamo, C.; Barone, V. *J. Chem. Phys.* **1999**, *110*, 6158.
- (65) Hod, O.; Barone, V.; Scuseria, G. E. *Phys. Rev. B* **2008**, *77*, 035411.
- (66) Jiang, D.; Sumpter, B. G.; Dai, S. *J. Chem. Phys.* **2008**, *127*, 124703.
- (67) Wittbrodt, J. M.; Schlegel, H. B. *J. Chem. Phys.* **1996**, *105*, 6574.
- (68) Montoya, A.; Truong, T. N.; Sarofim, A. F. *J. Phys. Chem. A* **2000**, *104*, 6108.
- (69) Pollet, R.; Amara, H. *J. Chem. Theory Comput.* **2009**, *5*, 1719.
- (70) Perdew, J. P.; Burke, K.; Ernzerhof, M. *Phys. Rev. Lett.* **1996**, *77*, 3865.
- (71) Merrick, J. P.; Moran, D.; Radom, L. *J. Phys. Chem. A* **2007**, *111*, 11683.
- (72) Inada, Y.; Orita, H. *J. Comput. Chem.* **2008**, *29*, 225.
- (73) Papas, B. N.; Schaefer, H. F. *J. Mol. Struct.* **2006**, *779*, 175.
- (74) Wang, H.; Xie, Y.; King, R. B.; Shaeffer, H. F. *J. Am. Chem. Soc.* **2005**, *127*, 11646.
- (75) Martin, J. M. L.; Bauschlicher, C. W.; Ricca, A. *Comput. Phys. Commun.* **2001**, *133*, 189.
- (76) Bauschlicher, C. W.; Peeters, E.; Allamandola, L. G. *Astrophys. J.* **2009**, *697*, 311, and references therein.
- (77) Joblin, C.; Boissel, P.; Léger, A.; d'Hendecourt, L.; Défourneau, D. *Astron. Astrophys.* **1995**, *299*, 835.
- (78) Salzmann, C. G.; Nicolosi, V.; Green, M. L. H. *J. Mater. Chem.* **2010**, *20*, 314.
- (79) Lenner, M.; Kaplan, A.; Huchon, Ch.; Palmer, R. E. *Phys. Rev. B* **2009**, *79*, 184105.

JP105728P